Res Chem Intermed
https://doi.org/10.1007/s11164-018-3315-2

Formation of hydroxyl radicals by α-Fe_2O_3 microcrystals and its role in photodegradation of 2,4-dinitrophenol and lipid peroxidation

Gilma Granados-Oliveros[1] · **Erika Torres**[2] · **Marcela Zambrano**[2] ·
Antonio Nieto-Camacho[3] · **Virginia Gómez-Vidales**[3]

Received: 9 October 2017 / Accepted: 30 January 2018

Abstract α-Fe_2O_3 microcrystals were produced for application as catalyst in different oxidation processes in both chemical and biological matrices. Hematite was produced by sol–gel method in situ with silica matrix and characterized by X-ray diffraction analysis, scanning electron microscopy with energy-dispersive X-ray spectrometry, and transmission electron microscopy. The ability of the catalyst to produce hydroxyl radicals (·OH) was evaluated by electron paramagnetic resonance measurements using 5,5-dimethyl- 1-pyrroline-*N*-oxide (DMPO) as spin trap. Characterization of the resulting DMPO-OH adduct established that α-Fe_2O_3 microcrystals could generate ·OH when Fenton chemistry was present. Additionally, the catalyst exhibited semiconducting properties, as the DMPO-OH signal was produced under visible-light irradiation in presence of O_2 but without requiring H_2O_2. In a pollution control context, 2,4-dinitrophenol (2,4-DNP) degradation was used as probe reaction, with >99 % of this pollutant being removed in presence of H_2O_2 under visible light. NO_2^-, NO_3^-, hydroxylated compounds, and a carboxylic acid were identified as photoproducts, suggesting a degradation pathway. Finally, catalyst reactivity in biological matrices was evaluated by oxidative degradation of

---

Electronic supplementary material The online version of this article (https://doi.org/10.1007/s11164-018-3315-2) contains supplementary material, which is available to authorized users.

✉ Gilma Granados-Oliveros
ggranadoso@unal.edu.co

[1] Nuevos Materiales Nano y Supramoleculares, Departamento de Química, Facultad de Ciencias, Universidad Nacional de Colombia, Bogotá, D.C., Colombia

[2] Facultad de Química Ambiental, Universidad Santo Tomás de Aquino, Bucaramanga, Colombia

[3] Instituto de Química, Universidad Nacional Autónoma de México, Circuito exterior, Ciudad Universitaria, 04510 Coyoacán, D.F., Mexico

lipids, revealing that α-Fe_2O_3 is a good oxidative stress inducer, representing a new application for materials based on iron oxides.

Keywords Hematite · Hydroxyl radicals · 2,4-DNP degradation · Lipid peroxidation · Visible light

Introduction

New catalytic methods involving environmentally friendly oxidants are needed to perform advanced oxidation of toxic and refractory aromatic pollutants. Although oxidation of pollutants can be realized by several homogeneous methodologies, for example, ultraviolet (UV)/H_2O_2, UV/H_2O_2/O_3, and UV/H_2O_2/Fe(II) or Fe(III) (photoassisted Fenton reaction) [1], the heterogeneous photo–Fenton process is an important alternative, offering various advantages such as low toxicity, good reuse capabilities, and stability [2]. In addition, unlimited solar energy can be efficiently harnessed. This process is based on formation of hydroxyl radicals ($^{\cdot}OH$), which are powerful oxidizing species in aqueous media with notable reactivity toward a wide variety of aromatic pollutants [3]. $^{\cdot}OH$ are produced from solid Fe species, H_2O_2, and UV irradiation, according to reactions 1 and 2, where $=Fe^{2+}$ and $=Fe^{3+}$ are iron species in solid phase or at the solid–liquid interface [4].

$$=Fe^{3+} - OH + h\nu \rightarrow =Fe^{2+} + {}^{\cdot}OH \tag{1}$$

$$=Fe^{2+} + H_2O_2 \rightarrow \left[=Fe^{3+} + OH^-\right] \left(e.g. =Fe^{3+} - OH\right) + {}^{\cdot}OH \tag{2}$$

Hematite (α-Fe_2O_3) is the most thermodynamically stable iron oxide phase, being an *n*-type semiconductor (bandgap energy, $E_g \approx 2.2$ eV); its absorption range includes a considerable portion of the solar spectrum [5], making it an interesting option for use in photocatalytic processes [4, 5]. This kind of process initiates when the surface of a semiconductor (in this case, hematite) is irradiated with energy greater than or equal to E_g, releasing electrons from the valence band (reaction 3) to conduction band. Photogenerated holes (h^+) react with water (reaction 4) and electrons (e^-) with oxygen (reaction 5) to form $^{\cdot}OH$ and superoxide radical anions, $O_2^{\cdot-}$, respectively [6]. However, hematite has a very short excited-state lifetime ($\sim$1 ps) [7] and short hole diffusion length ($\sim$2–4 nm) [8], resulting in undesirable electron–hole recombination [7] that affects the photocatalytic performance.

$$\alpha - Fe_2O_3 + h\nu \rightarrow h^+ + e^- \tag{3}$$

$$h^+ + H_2O \rightarrow {}^{\cdot}OH + H^+ \tag{4}$$

$$e^- + O_2 \rightarrow O_{2\cdot}^- \tag{5}$$

It has been shown that the efficiency of hematite depends on its crystalline structure [9], morphology, particle size, and surface area, which are related to the preparation method and starting materials [10–14]. α-Fe_2O_3 with high crystallinity can be easily synthesized using different techniques such as spray pyrolysis, hydrothermal, electrodeposition, and atmospheric-pressure chemical vapor deposition [15–24]. In situ preparation of α-Fe_2O_3 crystals in silica matrix is an inexpensive alternative, where the porous nature of the matrix provides sites for nucleation of the iron oxide particles, minimizes their aggregation, and suppresses interparticle interactions [7, 19–26].

The aim of this work is to evaluate the oxidizing properties of well-formed α-Fe_2O_3 particles in silica matrix under visible light. We used EPR measurements to evaluate the ability of α-Fe_2O_3 to produce $^{\cdot}OH$. In a pollution control context, the oxidant properties of this catalyst were studied for 2,4-DNP degradation, a toxic refractory chemical and carcinogenic environmental pollutant [27, 28]. This molecule is widely used in pesticide production, paints, and explosive materials, and has been detected not only in industrial wastewater but also in freshwater and marine environments [29]. Degradation of 2,4-DNP can be carried out by chemical oxidation [30], heterogeneous ozonation [31], electrochemical oxidation [32, 33], sonochemical methods [34, 35], and photocatalysis induced by UV [29] or visible light [36, 37]. In the case of hematite-based systems, removal of 2,4-DNP has been induced with UV light [38], but the mechanism involved in oxidation processes of this pollutant under visible light has yet not been reported.

Finally, to generate new applications of iron-based catalysts, specifically in the clinical field, we demonstrated that α-Fe_2O_3 microcrystals can induce lipid peroxidation. This kind of reaction is found as an intermediate process in many pathologies, such as cancers and neurodegenerative diseases [39].

Materials and methods

Reagents

Iron(III) chloride hexahydrate ($FeCl_3 \cdot 6H_2O$, >99.8 %), tetraethylorthosilicate (TEOS, 99.9 %), Griess reagent, oxalic acid dihydrate (99 %), ammonium metavanadate, vanadium(III) chloride, sodium nitrite (99 %), and sodium nitrate (99 %) were purchased from Sigma Chemical Co.; acetone, dichloromethane (99 %), and ethyl alcohol absolute (99.95 %) from J.T. Baker; hydroquinone (99 %) from Carlo Erba; glacial acetic acid (≥99.5 %), *p*-benzoquinone (99 %), 2,4-dinitrophenol (2,4-DNP, ≥97 %), potassium nitrate, and methanol (≥99.8 %) from Merck; 5,5-dimethyl-1-pyrroline-*N*-oxide (DMPO) of ultrahigh purity acquired from Dojindo; and water from a Millipore Waters Milli-Q water purification system were used.

Synthesis of α-Fe_2O_3 particles

α-Fe_2O_3 microcrystals were obtained by sol–gel method as follows [40]: 20 mmol $FeCl_3 \cdot 6H_2O$ and 42 mmol oxalic acid were dissolved in 40 mL ethanol by magnetic stirring at room temperature for 24 h, then the mixture was heated at 70 °C for 2 h.

A second solution was prepared by mixing 41.2 mmol TEOS [$Si(OC_2H_5)_4$] and 2.5 mmol potassium nitrate. This mix was subsequently added dropwise to solution containing iron chloride and oxalic acid with vigorous stirring at 80 °C. When homogeneous transparent solution was obtained, 100 mL water/ethanol (60/40 V/V) solution was added with vigorous stirring. Then, the reaction was heated at 100 °C for 16 h to give clear gel. The resulting gel was dried at 150 °C in vacuum for 24 h and calcined at 600 °C for 6 h in static air.

Catalyst characterization

Powder X-ray diffraction (XRD) analysis was performed using a Siemens D500 X-ray diffractometer with Cu K_α radiation source (140 V, 40 mA). The obtained pattern was compared with Joint Committee on Powder Diffraction Standards (JCPDS) data cards.

For scanning electron microscopy (SEM), a JEOL JSM-7600F was employed, and the energy-dispersive X-ray spectroscopy (EDX) spectrum was recorded using an Oxford Instruments INCA X-ACT microanalysis system. For transmission electron microscopy (TEM), a JEOL JEM-1200EX TEM operating at 200 kV was used. Average grain size was determined by computer-aided image analysis [ImageJ software, National Institutes of Health (NIH), Bethesda, MD, USA].

EPR measurements

Electron paramagnetic resonance (EPR) spectroscopy to detect hydroxyl radicals was carried out using a JEOL JES-TE300 EPR spectrometer, operated in X-band mode at modulation frequency of 100 kHz with a cylindrical cavity (TE_{011} mode), using parameters and experimental conditions similar to those previously reported [41] and described in detail in the Electronic Supporting Information.

Hydroxyl radicals generated by α-Fe_2O_3 were determined by using DMPO as spin trap. In a characteristic experiment, 20 mg catalyst was dispersed into 1 mL 30 mM DMPO aqueous solution by magnetic stirring for 1 h in the dark. O_2 was bubbled into the suspension for 30 min, then an aliquot of 200 μL was collected and placed into an EPR cell. The EPR signal was measured when 50 μmol H_2O_2 was added to the catalyst suspension. DMPO-OH was evaluated using the peak-height intensity of the second peak at room temperature. To confirm formation of $^{\cdot}OH$ by α-Fe_2O_3, 200 μL 1 M mannitol solution (a $^{\cdot}OH$ scavenger [42]) was added to catalyst suspension.

In photocatalytic experiments, suspensions of sample were irradiated for 5 min, directly in the EPR spectrometer microwave cavity, and EPR spectra were recorded in situ. A 1000-W Hg lamp (ES-USH10) equipped with a GG395 (Schott) optical filter (to eliminate UV wavelengths) was employed as irradiation system. The incident light flux (I_0) was measured by actinometry of potassium ferrioxalate [$K_3Fe(C_2O_4)_3 \cdot 3H_2O$] ($I_0 = 1.5 \times 10^{-5}$ mol L^{-1} s^{-1}) [43].

To determine the effect of dissolved oxygen on formation of $^{\cdot}OH$, α-Fe_2O_3 was added to DMPO solution in flowing nitrogen with magnetic stirring for 1 h, before initiating EPR measurements. In all experiments, pH was 7. Control experiments were also carried out, i.e., without/with catalyst, H_2O_2, or DMPO.

Determination of H_2O_2

Production of H_2O_2 from α-Fe_2O_3 suspensions was monitored by formation of a colored complex which can be measured by UV–Vis spectrophotometry at 450 nm (vanadate method [44]). Vanadate solution (0.060 M) was prepared by dissolving ammonium metavanadate (NH_4VO_3) in sulfuric acid solution (0.06 M) under magnetic stirring at 50 °C. The resulting solution was cooled and diluted with deionized water to obtain the desired concentration.

H_2O_2 concentration (mmol L^{-1}) was determined using a standard calibration; 0.2 mL vanadate solution was added to 0.2 mL H_2O_2 solutions (standards and aliquots from reaction). Spectrophotometric determinations were performed using an Agilent Technologies UV–Vis spectrophotometer with a 1-cm cell.

A typical procedure to produce H_2O_2 was as follows: α-Fe_2O_3 suspensions were prepared by adding 20 mg catalyst to 20 mL water. The mixture was magnetically stirred for 1 h before taking samples. O_2 was bubbled into the suspension, and the reactions were performed at room temperature. The irradiation conditions were the same as those employed in the EPR experiments. Aliquots of 0.2 mL were taken at regular times, then filtered through 0.45-μm nylon filters (Millipore) to remove catalyst particles and quantified using the vanadate solution as described above.

Degradation of 2,4-DNP

Degradation of pollutant was realized in a Pyrex cylindrical flask (80 mL capacity) equipped with a magnetic stirring bar and a water-circulating jacket. A 100-W halogen lamp (OSRAM, $\lambda \geq 390$ nm) was employed, and I_0 was 5.2×10^{-6} mol L^{-1} s^{-1} as determined by potassium ferrioxalate actinometry [43]. The emission spectrum of the light source is shown in the Electronic Supporting Information.

Degradation was achieved by adding 0.08 g catalyst to 80 mL 2,4-DNP (50 ppm) in aqueous solution with O_2 bubbled into the suspension. Then, the suspension was magnetically stirred in the dark for 1 h before irradiating to ensure adsorption/desorption equilibrium. All experiments were realized at pH ~7.0 (not controlled in the reactor) and room temperature. Some reactions were carried out in presence of H_2O_2 (0.01, 0.05, and 0.08 M). Reactions were monitored by collecting aliquots of the aqueous suspensions at regular times, which were filtered through 0.45-μm nylon filters (Millipore) and analyzed by high-performance liquid chromatography with diode array detector (HPLC–DAD).

Analytical determinations

HPLC analyses were carried out using an Agilent Technologies 1200 HPLC–DAD system and a ZORBAX SB C18 column (particle size 5 μm, 250 mm length × 4.6 mm i.d.) with a mixture of water (39 vol%), methanol (60 vol%), and acetic acid (1 vol%) as mobile phase at flow rate of 1 mL min^{-1}. The detection wavelength was 280 nm. These conditions were also employed to separate hydroquinone and benzoquinone as possible reaction intermediates; however, benzoquinone was not evidenced at the end of the reaction.

Gas chromatography (GC)–mass spectrometry (MS) analyses were performed on a Thermo Scientific ITQ 900 GC–MS system, with a capillary MEGA 5MS column (length 30 m, internal diameter 0.25 mm, film thickness 0.25 mm). Injection was carried out at 280 °C with split ratio of 9:1. The column temperature was held at 50 °C during 2 min, then raised at 10 °C min^{-1} to 280 °C, and finally held at 280 °C during 40 min. Electron ionization mass spectra were identified using the NIST 2002 library program with fit higher than 90 %.

Nitrite quantification

The amount of nitrite formed from 2,4-DNP degradation was quantified by Griess colorimetric method, which converts nitrite into a purple-colored azo compound that can be measured by UV–Vis spectrophotometry at 540 nm [45], using an Agilent Technologies UV–Vis spectrophotometer and a 1-cm cell. To determine nitrite, 1 g Griess reagent was dissolved in 25 mL deionized water. The nitrite $(NO_2)^-$ concentration (mmol L^{-1}) was determined using a standard calibration curve of $NaNO_2$. Griess solution (1 mL) was added to 1 mL solutions containing NO_2^- (standards and aliquots from 2,4-DNP degradation), and the absorbance was measured after 15 min.

Nitrate quantification

The amount of nitrate produced was also determined by Griess method, but nitrate was reduced to nitrite by acid solution of vanadium(III) according to the following procedure [46]: 0.5 g vanadium(III) chloride was dissolved in 200 mL HCl solution (0.5 M). Griess reagent (0.2 g) was added to VCl_3 solution. The nitrate $(NO_3)^-$ concentration (mmol L^{-1}) was determined using a standard calibration curve of $NaNO_3$. Vanadium(III) solution (1 mL) was added to 1 mL NO_3^- solutions (standards and aliquots from 2,4-DNP degradation), and the absorbance was measured at 540 nm after 24 h. In the case of aliquots, the nitrate concentration was calculated as the difference from the amount of formed nitrite.

Lipid peroxidation experiments

Lipid peroxidation by α-Fe_2O_3 microcrystals was studied by production of thiobarbituric acid reactive substances (TBARS). The subsequent procedures were previously described [41], and only minor modifications were made (see Electronic Supporting Information for more details).

Results and discussion

Characterization of catalyst

Figure 1a shows the XRD pattern of α-Fe_2O_3 sample, which can be assigned to rhombohedral phase (JCPDS no. 33-664). The strong and sharp diffraction peaks indicate good crystallinity of the synthesized α-Fe_2O_3 [47]. No other diffraction peaks were observed, indicating that SiO_2 was in amorphous state, as also observed in a previous report [48].

Figure 1b shows a SEM image of the sample. Hematite single crystals with elongated shape and average length of 1.15 ± 0.39 μm were obtained upon annealing at 600 °C. Since the α-Fe_2O_3 microcrystals were developed in situ with silica matrix by hydrolysis and condensation of TEOS, the porous silica nanostructure before the calcination process can be appreciated by SEM (see Electronic Supporting Information). The chemical composition determined by EDX analysis confirmed that Si, O, and Fe were the only elements contained within the catalyst (Fig. 1c). The sample was further examined by TEM (Fig. 1d); the difference in contrast between darker and lighter areas indicates silica dispersed on α-Fe_2O_3 microcrystals.

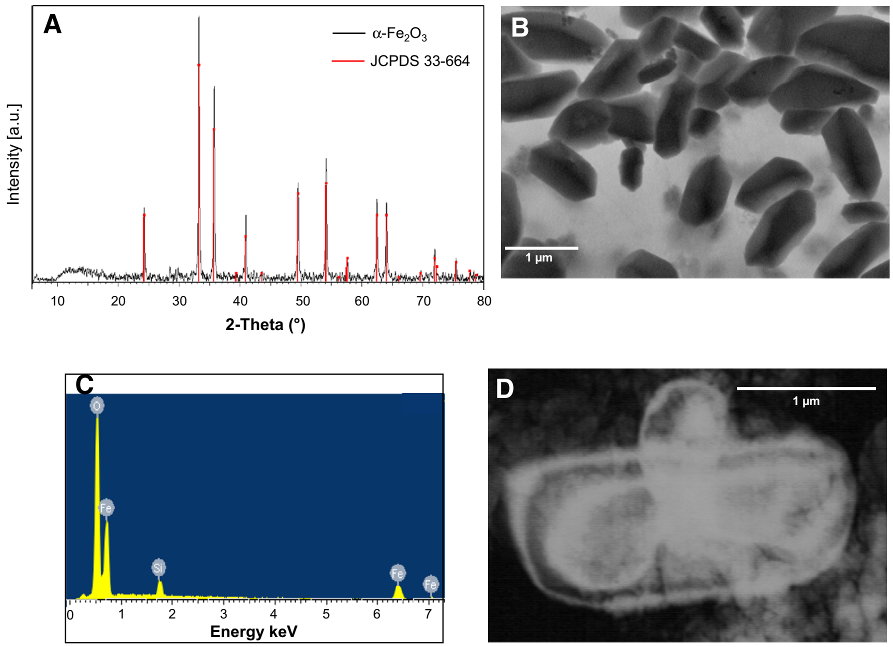

Fig. 1 **a** XRD pattern of α-Fe_2O_3 prepared in presence of SiO_2; red lines indicate positions of standard peaks of hematite α-Fe_2O_3 (JCPDS 33-664). **b** SEM image, **c** EDX analysis, and **d** TEM image of α-Fe_2O_3 microcrystals

EPR analysis

We employed DMPO as a free-radical trap to provide evidence of the formation of hydroxyl radicals from α-Fe_2O_3 in oxygenated aqueous suspension, at room temperature under visible-light irradiation. In dark conditions, no signal was observed for the catalyst in presence of DMPO (Fig. 2a); however, when H_2O_2 was added to the suspension, the DMPO-OH adduct signal was observed, indicating generation of $^{\cdot}OH$ (Fig. 2b). This signal exhibits four strong splitting lines with intensity ratio of 1:2:2:1 ratio and hyperfine splitting constant (hfsc) of $a_N = a_H = 14.9$ G and $g = 2.0057$ [49, 50]. Control experiments showed that catalyst and H_2O_2 were indispensable for production of the DMPO-OH adduct signal. The role of dissolved O_2 was evaluated by bubbling nitrogen through the suspension. In this condition, signal intensity slightly decreased (Fig. 2c), in comparison with Fig. 2b, suggesting that O_2 is not essential to produce $^{\cdot}OH$.

To confirm $^{\cdot}OH$ formation from catalyst suspensions in presence of H_2O_2, the effect of mannitol as $^{\cdot}OH$ scavenger [51] was determined. In this circumstance, the intensity of DMPO-OH adduct signal was clearly inhibited by mannitol (Fig. 2d), demonstrating that $^{\cdot}OH$ was effectively formed. These results suggest that H_2O_2 is necessarily required to produce $^{\cdot}OH$ by α-Fe_2O_3 microcrystals, via reactions 6 followed by reaction 2, in accordance with a heterogeneous Fenton reaction [52].

$$=Fe^{3+} + H_2O_2 \rightarrow =Fe^{2+} + H^+ + HO_2^{\cdot} \tag{6}$$

Figure 3 shows the photoinduced formation of $^{\cdot}OH$ by the catalyst. After irradiation with visible light ($\lambda > 400$ nm) for 5 min, oxygenated aqueous suspension containing α-Fe_2O_3 particles could produce the DMPO-OH adduct without H_2O_2 as prerequisite (Fig. 3a). When N_2 was bubbled through the suspension to remove dissolved oxygen from solution, the DMPO-OH signal was affected (Fig. 3b). In addition, we evaluated the effect of H_2O_2 (0.05 M) on formation of hydroxyl radicals by catalyst, finding that the adduct signal was dramatically increased (Fig. 3c). No DMPO-OH adduct was produced in presence of H_2O_2 but without hematite under irradiation (Fig. 3d).

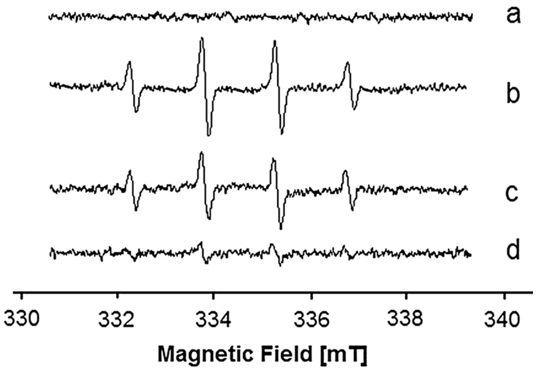

Fig. 2 EPR spectra of DMPO-OH adduct from α-Fe_2O_3 in oxygenated aqueous suspensions (1 g L^{-1}) in dark condition and under several experimental conditions: **a** without H_2O_2, **b** with H_2O_2, **c** with H_2O_2 and N_2, and **d** in presence of mannitol

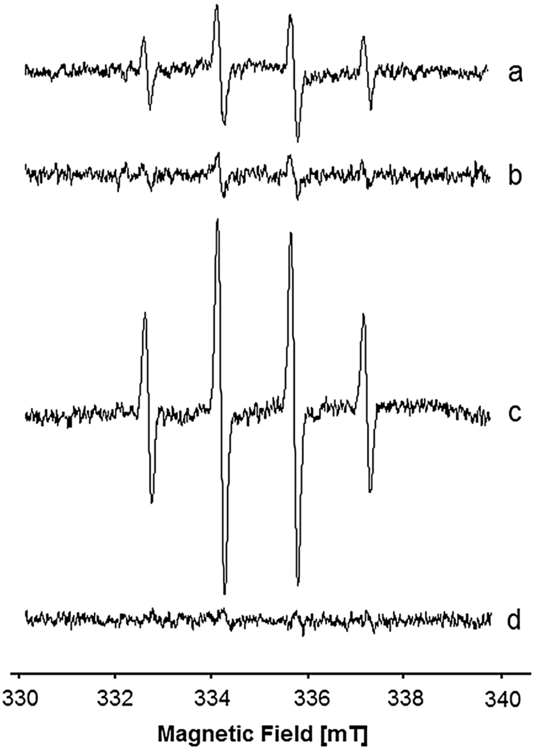

Fig. 3 DMPO spin-trapping EPR spectra from α-Fe_2O_3 microcrystals in oxygenated aqueous suspensions (1 g L^{-1}) under visible-light irradiation: **a** without H_2O_2, **b** with N_2 and without H_2O_2, **c** with H_2O_2, and **d** without catalyst: DMPO alone, DMPO + H_2O_2

Based on all these observations, we hypothesized that photoproduction of $^{\cdot}OH$ by visible light could occur via two main paths: (1) via heterogeneous photo-Fenton reaction, which would require H_2O_2 to produce $^{\cdot}OH$ (reactions 1 and 2), and (2) formation of $O_2^{\cdot-}$ after hematite excitation (reaction 5). These species are very reactive, and through a disproportionation process produce H_2O_2 and then $^{\cdot}OH$ (reactions 7–9) [53]. The strong production of $^{\cdot}OH$ by α-Fe_2O_3 microcrystals under visible-light irradiation results by combining these paths.

$$2O_{2\cdot}^{-} + 2H^{+} \rightarrow H_2O_2 + O_2 \tag{7}$$

$$H_2O_2 + O_{2\cdot}^{-} \rightarrow {}^{\cdot}OH + OH^{-} + O_2 \tag{8}$$

$$H_2O_2 + e^{-} \rightarrow {}^{\cdot}OH + OH^{-} \tag{9}$$

Because H_2O_2 may be produced as an intermediate (reaction 7), we determined the amount of H_2O_2 formed in the reaction. Figure 4 shows the formation of hydrogen peroxide by α-Fe_2O_3 in dark condition and upon visible-light irradiation ($\lambda > 400$ nm). No formation of H_2O_2 was detected in dark conditions, but when α-Fe_2O_3 dispersions were irradiated, production of H_2O_2 increased to 28 µM. After this, the amount of H_2O_2 decreased, possibly due to reactions 8–9. We emphasize that the photogenerated H_2O_2 was sufficient to produce a detectable amount of

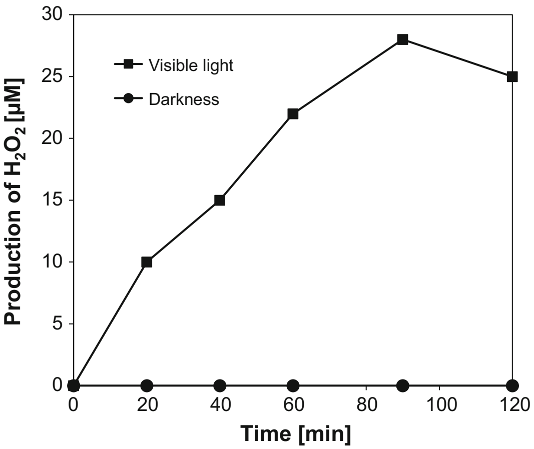

Fig. 4 Photoproduction of H_2O_2 versus reaction time by α-Fe_2O_3 catalyst under visible-light irradiation in comparison with dark condition

hydroxyl radicals (Fig. 3a), confirming the capacity of α-Fe_2O_3 microcrystals to produce reactive species under visible-light illumination.

Furthermore, the photoinduced formation of $^{\cdot}OH$ from α-Fe_2O_3 (without H_2O_2) could also indicate a low rate of hole–electron recombination. In this context, heterostructures with different bandgaps such as α-Fe_2O_3/TiO_2 [54], α-Fe_2O_3/SiO_2 [13], and Fe_2O_3/ZnO [55] are helpful to suppress recombination of photogenerated charges, facilitating charge separation. This property maximizes its potential for use as photocatalyst.

Degradation of 2,4-dinitrophenol under visible light

Figure 5 shows the role of α-Fe_2O_3 microcrystals as Fenton-type catalyst and photocatalyst. In dark condition (Fig. 5a), no degradation of 2,4-DNP was observed by the catalyst alone. However, pollutant degradation in presence of hematite and H_2O_2 was observed, although the kinetics remained slow since less than 10 % of the substrate was degraded within 1 h of reaction. These results are in accordance with the EPR results, insomuch as α-Fe_2O_3 in presence of H_2O_2 produces $^{\cdot}OH$ to start the degradation process. However, low activity for degradation of this organic pollutant in dark condition is evident. This finding is consistent with the low Fenton reactivity reported for material surfaces containing Fe(III) [56].

Figure 5b shows the degradation of 2,4-DNP using α-Fe_2O_3 particles after visible-light irradiation for 2 h. Owing to its semiconducting properties, α-Fe_2O_3 in presence of O_2 could achieve up to 16 % degradation of the pollutant. This result is in accordance with the EPR results, since $^{\cdot}OH$ could be formed without H_2O_2.

Substantial degradation (>99 %) was obtained when H_2O_2 (0.05 M) was added to hematite suspensions, confirming its involvement in a heterogeneous photo-Fenton process induced by visible light. Control experiments were also carried out, revealing that direct photolysis of pollutant and photodegradation by H_2O_2 (without catalyst in both cases) were negligible. 2,4-DNP degradation was around 80 %

Fig. 5 Degradation of 2,4-DNP versus reaction time using α-Fe_2O_3 catalyst: **a** in dark condition, and **b** under visible-light irradiation. [2,4-DNP] = 50 ppm; [H_2O_2] = 0.05 M, catalyst = 1 g L^{-1}. Δ Control experiments without catalyst: pollutant alone, pollutant + H_2O_2

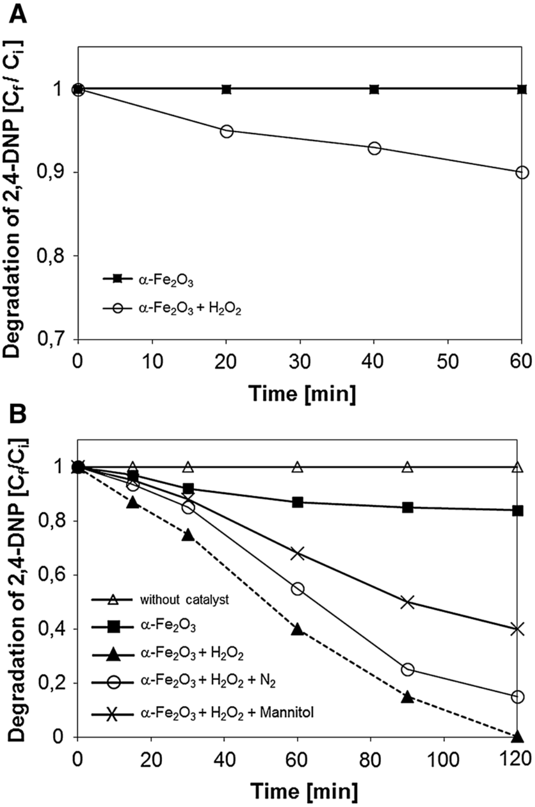

when the reaction was realized without O_2, revealing that, to achieve advanced oxidation more quickly, H_2O_2 and molecular oxygen are required.

To evaluate the role of $^{\cdot}OH$ in the photodegradation process, an experiment with mannitol (a $^{\cdot}OH$ scavenger) was carried out. In this situation, the degradation was 55 %, confirming that $^{\cdot}OH$ is indeed involved in the total degradation of this toxic and recalcitrant pollutant.

To assess the effect of H_2O_2, 2,4-DNP degradation was realized with different amounts of H_2O_2 (Fig. 6). According to the results, increasing the H_2O_2 concentration to 0.05 M increased the 2,4-DNP degradation. However, at higher H_2O_2 concentration (0.08 M), the degradation decreased. In this case, the reaction may be inhibited by H_2O_2 overdose (reactions 10 and 11), where the reaction between H_2O_2 and $^{\cdot}OH$ produces peroxyl radicals ($HO_2^{\cdot}$) with lower oxidation potential than hydroxyl radicals, consequently affecting the degradation of 2,4-DNP [57].

$$H_2O_2 + {}^{\cdot}OH \rightarrow HO_2^{\cdot} + H_2O \tag{10}$$

$$HO_2{\cdot} + {}^{\cdot}OH \rightarrow H_2O + O_2 \tag{11}$$

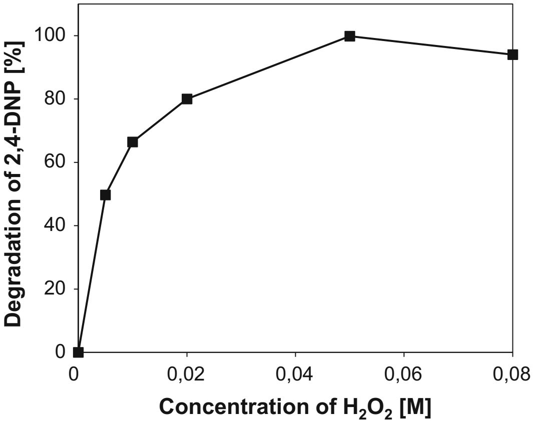

Fig. 6 Effect of H_2O_2 concentration on 2,4-DNP photodegradation

Photoproducts

Hydroxyl radicals can attack 2,4-DNP, leading to release of the nitro group [58]. This was evaluated by the formation of nitrite (NO_2^-) and nitrate (NO_3^-) anions, which were estimated as the percentage of the initial amount of nitrogen, given initial concentration of 50 ppm (0.27 mM), i.e., $[N]_0 = 0.54$ mM (Eqs. 12 and 13):

$$NO_2^- \text{ in } \%N = \frac{NO_2^-}{N_0} \times 100 \quad (12)$$

$$NO_3^- \text{ in } \%N = \frac{NO_3^-}{N_0} \times 100 \quad (13)$$

Figure 7 shows the evolution of NO_2^- and NO_3^- as photoproducts of 2-4-DNP degradation. According to these results, in dark condition, less than 10 % of 2,4-DNP was degraded by α-Fe_2O_3, in presence of H_2O_2 (0.05 M), so an amount of NO_2^- (10 μM) and NO_3^- (25 μM) could be detected, evidencing that the 2,4-DNP degradation process took place. During irradiation, the nitrite concentration increased to 28 μM, equivalent to 5 % considering the ratio of inorganic to total nitrogen. Meanwhile, the nitrate concentration reached a maximum of 450 μM, corresponding to 80.4 % (see inset in Fig. 7) of the nitro group detached. Nitrite could be transformed into NO_3^- by secondary reactions, which could explain the small amount of NO_2^- formed in the course of the reaction. It is known that nitrites can act as efficient scavengers of $^{\cdot}OH$ to produce $\cdot NO_2$ species (reaction 14) [59]. Furthermore, $^{\cdot}NO_2$ is not a stable intermediate in aqueous solution, as it undergoes fast dimerization (reaction 15) and hydrolysis (reaction 16), producing NO_3^- [47, 49].

$$NO_2^- + {}^{\cdot}OH \rightarrow {}^{\cdot}NO_2 + OH^- \quad (14)$$

$$2\,{}^{\cdot}NO_2 \rightleftarrows N_2O_4 \quad (15)$$

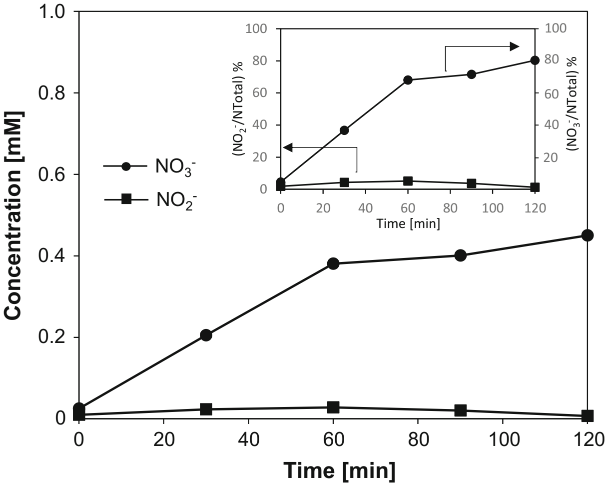

Fig. 7 Time evolution of nitrite and nitrate ions in 2,4-DNP photodegradation by hematite microcrystals in presence of H_2O_2 induced with visible light. Inset: ratio of inorganic to total nitrogen as function of time

$$N_2O_4 + H_2O \rightarrow HNO_2 + NO_3^- + H^+ \tag{16}$$

On the other hand, >99 % of 2,4-DNP was transformed. Table 1 presents the intermediates generated during the photocatalytic process, as detected by GC–MS. Figure 8 shows the formation pathway of these intermediates and confirms the presence of hydroxyl radicals. Indeed, 2,4-DNP degradation seems to be initiated by $^{\cdot}OH$ attack preferentially at those positions with higher electron density, viz. denitration from aromatic rings, followed by addition of hydroxyl group to ring, producing hydroxylated intermediates. Subsequently, ring cleavage took place, leading to formation of 2-pentenedioic acid and a variety of carboxylic acids (such as maleic, malic, oxalic, acetic, and formic) which were not identified in the present case but have been detected as products of 2,4-DNP degradation by other systems [33, 58]. According to literature, hydroxylated intermediates and carboxylic acids could be finally oxidized to CO_2 and H_2O [60].

TBARS production

To generate new applications, especially in the clinical field, we used rat brain homogenate as a biological substrate to evaluate the activity of α-Fe_2O_3 microcrystals as inducers of lipid peroxidation (LP), measured by TBARS production [41]. Figure 9 shows the TBARS production with the catalyst as a function of incubation time (t_i), used to identify when a significant LP level was achieved by the catalyst, with $t_i = 0$ h as reference. These results indicate that α-Fe_2O_3 particles could induce TBARS production, becoming significant ($p \leq 0.05$) at $t_i \geq 2$ h. Subsequent experiments were realized with $t_i = 3$ h. TBARS production is consistent with Fenton chemistry where addition of H_2O_2 to α-Fe_2O_3

Table 1 Detected photoproducts by GC–MS

Rt	m/z	Compound
14.0	130	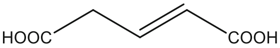
16.6	108	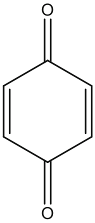
19.4	110	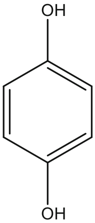
22.0	139	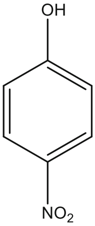
25.4	155	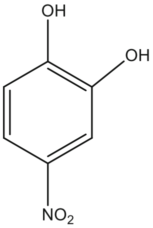 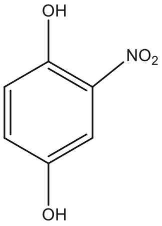

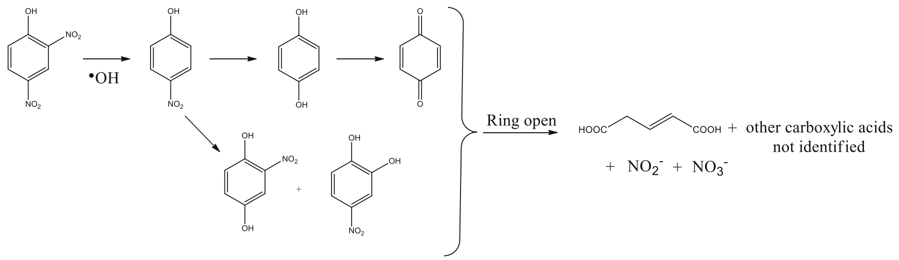

Fig. 8 Possible pathway for intermediate of 2,4-DNP photodegradation by α-Fe_2O_3 microcrystals in presence of H_2O_2 and visible light

Fig. 9 Effect of incubation time on TBARS formation in α-Fe_2O_3 suspensions and brain homogenate only (both at 1000 mg mL^{-1}), with statistical significance for $p \leq 0.05$ (*) and $p \leq 0.01$ (**) values

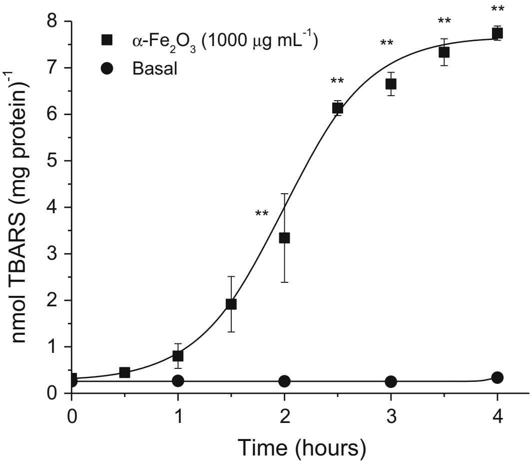

suspensions is required to produce $^{\cdot}OH$ (reactions 6 and 2). Albeit at low amounts, brain contains lipid hydroperoxides (LO_2H) as activity products of lipoxygenase (LOX), cyclooxygenase (COX), cytochrome c-450 enzymes, cytochrome c, and myeloperoxidase (MPO), among others [61, 62]. Lipid hydroperoxides can react with iron of α-Fe_2O_3 particles by reaction 17, in an analogous way to reaction 6, producing the lipid peroxyl radical ($LO_2^{\cdot}$) which can participate in the chain of lipid peroxidation propagation [61, 63].

$$=Fe^{3+} + LO_2H \rightarrow = Fe^{2+} + H^+ + LO_2^{\cdot} \tag{17}$$

The effect of the α-Fe_2O_3 concentration on the TBARS formation is shown in Fig. 10. The TBARS production increased as the catalyst concentration was increased, becoming significant ($p \leq 0.001$) at 200 μg mL^{-1} and reaching a maximum at 1000 μg mL^{-1}. The lipid peroxidation was significant and more active than that induced by 2,2′-azobis(2-amidinopropane) dihydrochloride (AAPH, a typical free-radical generator, capable of inducing LP [62]). Thus, the catalyst can be considered to be an effective oxidative stress inducer. α-Fe_2O_3 microcrystals in presence of H_2O_2 showed strong activity in Fenton reactions due to the ability to

Fig. 10 Effect of α-Fe_2O_3 concentration on TBARS formation. Statistical significance for $p \leq 0.01$ (**)

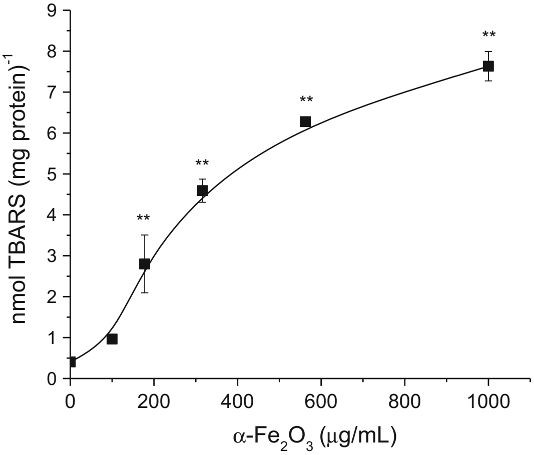

form hydroxyl radicals. However, we highlight the fact that the activity in biological matrices was more efficient than in chemical matrices (Fig. 5a).

Such exploration of new applications for iron-based heterostructures is particularly interesting for the clinical area, since LP plays a crucial role in treatment of multiple pathologies, such as cancers and degenerative diseases of the brain and central nervous system [39].

Conclusions

Catalytic applications of α-Fe_2O_3 microcrystals were studied. The ability of this catalyst to produce reactive intermediates such as $^{\cdot}OH$ and H_2O_2 under visible-light irradiation was evidenced. These properties were exploited for degradation of 2,4-DNP initiated by $^{\cdot}OH$, generating release of nitro group, hydroxylated photoproducts, and aromatic ring cleavage. Based on the detected products, a degradation pathway was proposed.

In addition, α-Fe_2O_3 showed excellent properties for use in therapeutic applications, given its ability to induce lipid peroxidation and oxidative stress.

Acknowledgements This work was supported by DIEB, UNAL (QUIPU code 201010025976). The authors thank Claudia Rivera Cerecedo and Héctor Malagón Rivero from the Instituto de Fisiología at UNAM for donation of biological samples.

References

1. S. Esplugas, J. Giménez, S. Contreras, E. Pascual, M. Rodríguez, Water Res. **36**, 1034 (2002)
2. J. Herney-Ramirez, M.A. Vicente, L.M. Madeira, Appl. Catal. B Environ. **98**, 10 (2010)
3. J.J. Pignatello, E. Oliveros, A. MacKay, Crit. Rev. Environ. Sci. Technol. **36**, 1 (2006)
4. C. Wang, H. Liu, Z. Sun, J. Huag, Y. Liao, Int. J. Photoenergy **2012**, 1 (2012)
5. W. Du, Y. Xu, Y. Wang, Langmuir **24**, 175 (2008)

6. R. Sugrañez, J. Balbuena, M. Cruz-Yusta, F. Martín, J. Morales, L. Sánchez, Appl. Catal. B Environ. **165**, 529 (2015)
7. A.G. Joly, J.R. Williams, S.A. Chambers, G. Xiong, W.P. Hess, D.M. Laman, J. Appl. Phys. **99**, 53521 (2006)
8. J.H. Kennedy, K.W. Frese, J. Electrochem. Soc. **125**, 709 (1978)
9. Y. Wang, W. Du, Y. Xu, Langmuir **25**, 2895 (2009)
10. X. Zhang, Y. Niu, Y. Li, X. Hou, Y. Wang, R. Bai, J. Zhao, Mater. Lett. **99**, 111 (2013)
11. X. Liu, K. Chen, J.-J. Shim, J. Huang, J. Saudi Chem. Soc. **19**, 479 (2015)
12. D.A. Wheeler, G. Wang, Y. Ling, Y. Li, J.Z. Zhang, Energy Environ. Sci. **5**, 6682 (2012)
13. K. Cheng, Y.P. He, Y.M. Miao, B.S. Zou, Y.G. Wang, T.H. Wang, X.T. Zhang, Z.L. Du, J. Phys. Chem. B **110**, 7259 (2006)
14. T. Meng, P. Xie, H. Qin, H. Liu, W. Hua, X. Li, Z. Ma, J. Mol. Catal. A Chem. **421**, 109 (2016)
15. J.-P. Jolivet, C. Chanéac, E. Tronc, Chem. Commun. **5**, 477 (2004)
16. L. Machala, J. Tuček, R. Zbořil, Chem. Mater. **23**, 3255 (2011)
17. M. Tadic, V. Kusigerski, D. Markovic, I. Milosevic, V. Spasojevic, J. Magn. Magn. Mater. **321**, 12 (2009)
18. L.L. Hench, J.K. West, Chem. Rev. **90**, 33 (1990)
19. L. Casas, A. Roig, E. Molins, J.M. Grenèche, J. Asenjo, J. Tejada, Appl. Phys. A **74**, 591 (2002)
20. A.K. Gupta, M. Gupta, Biomaterials **26**, 3995 (2005)
21. Y. Yang, H. Ma, J. Zhuang, X. Wang, Inorg. Chem. **50**, 10143 (2011)
22. Q. Xiang, G. Chen, T.-C. Lau, RSC Adv. **5**, 52210 (2015)
23. J. Zhao, H.-S. Chen, K. Matras-Postolek, P. Yang, CrystEngComm **17**, 7175 (2015)
24. X. Hu, J.C. Yu, J. Gong, Q. Li, G. Li, Adv. Mater. **19**, 2324 (2007)
25. G. Encheva, B. Samuneva, P. Djambaski, E. Kashchieva, D. Paneva, I. Mitov, J. Non. Cryst. Solids **345–346**, 615 (2004)
26. L. Machala, R. Zboril, A. Gedanken, J. Phys. Chem. B **111**, 4003 (2007)
27. R. Blasco, F. Castillo, Pestic. Biochem. Physiol. **58**, 1 (1997)
28. R. Belloli, E. Bolzacchini, L. Clerici, B. Rindone, G. Sesana, V. Librando, Environ. Eng. Sci. **23**, 405 (2006)
29. S.S. Shukla, K.L. Dorris, B.V. Chikkaveeraiah, J. Hazard. Mater. **164**, 310 (2009)
30. P. Zhou, J. Zhang, Y. Zhang, G. Zhang, W. Li, C. Wei, J. Liang, Y. Liu, S. Shu, J. Hazard. Mater. **344**, 1209 (2018)
31. Y. Dadban Shahamat, M. Sadeghi, A. Shahryari, N. Okhovat, F. Bahrami Asl, M.M. Baneshi, Desalin. Water Treat. **57**, 20447 (2016)
32. Y. Liu, H. Liu, J. Ma, X. Wang, Appl. Catal. B Environ. **91**, 284 (2009)
33. M.A. Quiroz, J.L. Sánchez-Salas, S. Reyna, E.R. Bandala, J.M. Peralta-Hernández, C.A. Martínez-Huitle, J. Hazard. Mater. **268**, 6 (2014)
34. Z. Guo, R. Feng, J. Li, Z. Zheng, Y. Zheng, J. Hazard. Mater. **158**, 164 (2008)
35. M.V. Bagal, B.J. Lele, P.R. Gogate, Ultrason. Sonochem. **20**, 1217 (2013)
36. M. Myilsamy, M. Mahalakshmi, V. Murugesan, N. Subha, Appl. Surf. Sci. **342**, 1 (2015)
37. X. Chen, Y. Liu, X. Xia, L. Wang, Appl. Surf. Sci. **407**, 470 (2017)
38. E.M. Seftel, M. Puscasu, M. Mertens, P. Cool, G. Carja, Catal. Today **252**, 7 (2015)
39. M.M. Gaschler, B.R. Stockwell, Biochem. Biophys. Res. Commun. **482**, 419 (2017)
40. A.A. Mirzaei, A.B. Babaei, M. Galavy, A. Youssefi, Fuel Process. Technol. **91**, 335 (2010)
41. G. Granados-Oliveros, V. Gomez-Vidales, A. Nieto-Camacho, J.A. Morales-Serna, J. Cardenas, M. Salmon, RSC Adv. **3**, 937 (2013)
42. G. Granados-Oliveros, E.A. Páez-Mozo, F.M. Ortega, C. Ferronato, J.M. Chovelon, Appl. Catal. B Environ. **89**, 448 (2009)
43. T. Lehóczki, É. Józsa, K. Ösz, J. Photochem. Photobiol. A Chem. **251**, 63 (2013)
44. R.F.P. Nogueira, M.C. Oliveira, W.C. Paterlini, Talanta **66**, 86 (2005)
45. A. Kiss, L. Juhász, G. Seprényi, K. Kupai, J. Kaszaki, Á. Végh, Br. J. Pharmacol. **160**, 1263 (2010)
46. T.A. Doane, W.R. Horwáth, Anal. Lett. **36**, 2713 (2003)
47. R.M. Cornell, U. Schwertmann, *Iron Oxides* (Wiley-VCH, New York, 2004), p. 365
48. C. Păcurariu, E.-A. Tăculescu (Moacă), R. Ianoş, O. Marinică, C.-V. Mihali, V. Socoliuc, Ceram. Int. **41**, 1079 (2015)
49. A.S.W. Li, C.F. Chignell, J. Biochem. Biophys. Methods **22**, 83 (1991)
50. S. Tero-Kubota, Y. Ikegami, T. Kurokawa, R. Sasaki, K. Sugioka, M. Nakano, Biochem. Biophys. Res. Commun. **108**, 1025 (1982)

51. K.K. Mothilal, J. Johnson Inbaraj, R. Gandhidasan, R. Murugesan, J. Photochem. Photobiol. A Chem. **162**, 9 (2004)
52. C. Hammond, M.M. Forde, M.H. Ab Rahim, A. Thetford, Q. He, R.L. Jenkins, N. Dimitratos, J.A. Lopez-Sanchez, N.F. Dummer, D.M. Murphy, A.F. Carley, S.H. Taylor, D.J. Willock, E.E. Stangland, J. Kang, H. Hagen, C.J. Kiely, G.J. Hutchings, Angew. Chem. Int. Ed. **51**, 5129 (2012)
53. P. Pichat, C. Guillard, L. Amalric, A.-C. Renard, O. Plaidy, Sol. Energy Mater. Sol. Cells **38**, 391 (1995)
54. X. Zhang, L. Lei, Appl. Surf. Sci. **254**, 2406 (2008)
55. S. Si, C. Li, X. Wang, Q. Peng, Y. Li, Sensors Actuators B Chem. **119**, 52 (2006)
56. W. Huang, M. Brigante, F. Wu, K. Hanna, G. Mailhot, Environ. Sci. Pollut. Res. **20**, 39 (2013)
57. I. Muthuvel, M. Swaminathan, Sol. Energy Mater. Sol. Cells **92**, 857 (2008)
58. Y. Liu, H. Liu, J. Ma, X. Wang, Appl. Catal. B Environ. **91**, 284 (2009)
59. J.A. Herrera-Melián, A.J. Martín-Rodríguez, A. Ortega-Méndez, J. Araña, J.M. Doña-Rodríguez, J. Pérez-Peña, J. Environ. Manag. **105**, 53 (2012)
60. L. Demarchis, M. Minella, R. Nisticò, V. Maurino, C. Minero, D. Vione, J. Photochem. Photobiol. A Chem. **307–308**, 99 (2015)
61. T.S. Anthonymuthu, E.M. Kenny, H. Bayır, Brain Res. **1640**, 57 (2016)
62. E. Niki, Free Radic. Biol. Med. **47**, 469 (2009)
63. Z. Cheng, Y. Li, Chem. Rev. **107**, 2165 (2007)